



Cite this: *Soft Matter*, 2019,  
15, 1053

# A comparison of the network structure and inner dynamics of homogeneously and heterogeneously crosslinked PNIPAM microgels with high crosslinker content†

Judith Witte,  <sup>a</sup> Tetyana Kyrey, <sup>abc</sup> Jana Lutzki, <sup>a</sup> Anna Margarethe Dahl, <sup>a</sup> Judith Houston,  <sup>b</sup> Aurel Radulescu, <sup>b</sup> Vitaliy Pipich, <sup>b</sup> Laura Stingaciu, <sup>d</sup> Matthias Kühnhammer, <sup>c</sup> Marcus U. Witt, <sup>c</sup> Regine von Klitzing, <sup>c</sup> Olaf Holderer <sup>b</sup> and Stefan Wellert <sup>a</sup>

Poly(*N*-isopropylacrylamide) microgel particles were prepared via a “classical” surfactant-free precipitation polymerization and a continuous monomer feeding approach. It is anticipated that this yields microgel particles with different internal structures, namely a dense core with a fluffy shell for the classical approach and a more even crosslink distribution in the case of the continuous monomer feeding approach. A thorough structural investigation of the resulting microgels with dynamic light scattering, atomic force microscopy and small angle neutron scattering was conducted and related to neutron spin echo spectroscopy data. In this way a link between structural and dynamic features of the internal polymer network was made.

Received 20th October 2018,  
Accepted 26th December 2018

DOI: 10.1039/c8sm02141d

rsc.li/soft-matter-journal

## 1 Introduction

Microgel particles, especially those with responsive properties such as thermoresponsivity, pH-responsivity or responsivity to ionic strength are the object of numerous scientific investigations due to their large potential for applications such as drug delivery,<sup>1–3</sup> sensoric applications<sup>4–7</sup> or biotechnological applications.<sup>8–10</sup> *N*-Isopropylacrylamide (NIPAM) is a widely used monomer for the synthesis of said microgel particles. A lower critical solution temperature (LCST) of the NIPAM monomer of approximately 32 °C leads to a similar volume phase transition temperature (VPTT) for poly(*N*-isopropylacrylamide) (PNIPAM) microgel particles. Factors that may influence the VPTT are the use of a comonomer with a different LCST<sup>11</sup> or the functionalization of the polymer network.<sup>12</sup> Those strategies therefore enable the synthesis of microgel particles with a tunable VPTT.

*N,N'*-Methylenebisacrylamide (BIS) is commonly used as a crosslinker in PNIPAM microgels. It was found by Wu *et al.* that during emulsion polymerization BIS molecules are consumed faster than NIPAM molecules.<sup>13</sup> This results in an uneven distribution of crosslinking and hence in a denser core and a fluffier shell.<sup>14</sup>

To tune the microgel structure towards a more even distribution of crosslinks and polymer, several procedures of introducing the crosslinker and monomers into the network have been tested. For example, semibatch reaction processes were found to lead to a homogeneous morphology.<sup>15,16</sup>

Beside this, it was demonstrated that droplet based microfluidic templating enables the formation of microgels with different inner homogeneity and sizes of several ten to hundreds of micrometers.<sup>17,18</sup> By choosing a monomer feeding approach for the PNIPAM microgel particles it has been attempted to circumvent this problem and achieve an even distribution of crosslinks in sub micrometer sized microgels. Most publications take studies of optical properties such as transparency/turbidity and dynamic light scattering as an evidence for the homogeneous crosslinking of the PNIPAM microgel particles.<sup>19,20</sup> Although supporting the conclusion of a homogeneous inner structure, these methods provide no direct access to the inner structural properties. Theoretical considerations and experiments using dielectric spectroscopy<sup>21,22</sup> predict an influence of the microstructure of the microgels on their physico-chemical properties, *e.g.*, swelling kinetics<sup>23</sup> and desired functionality.<sup>24</sup>

<sup>a</sup> Institute of Chemistry, TU Berlin, Strasse des 17. Juni 124, 10623 Berlin, Germany. E-mail: judith.witte@tu-berlin.de; Fax: +49 30 31426602; Tel: +49 30 31426774

<sup>b</sup> Jülich Centre for Neutron Science JCNS, Forschungszentrum Jülich GmbH, Outstation at MLZ, Lichtenbergstrasse 1, 85747 Garching, Germany

<sup>c</sup> Institute of Physics, TU Darmstadt, Alarich-Weiss-Strasse 10, 64287 Darmstadt, Germany

<sup>d</sup> NScD, Oak Ridge National Laboratory, Oak Ridge, Tennessee 37831, USA

† Electronic supplementary information (ESI) available. See DOI: 10.1039/c8sm02141d



Besides this, the interaction potential between them, their ability to interpenetrate and their behavior at very dense packing conditions are influenced, *e.g.*, by the microgel softness and the internal crosslinker density distribution.<sup>25,26</sup>

Hence, a thorough and direct comparison of the internal structure and dynamics of both types of microgels in the often investigated sub micrometer size range is of importance but still missing. In case of inhomogeneity-free macroscopic gels, differences in the network dynamics compared to heterogeneous gels were found in a combined light and neutron scattering study.<sup>27</sup>

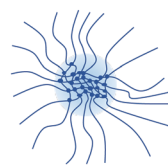
Very recently, it was shown that super-resolution microscopy methods can probe the inner network morphology by indirect or direct labeling. Here, the proportionality between the localization distribution of the probe and the network was used.<sup>28,29</sup> Also, photoactivation localization microscopy (PALM) on microgel particles synthesized *via* precipitation polymerization with the addition of a photochromic diarylethene photoswitch as crosslinker allows a 3D reconstruction of the distribution of crosslinker positions in a microgel in its hydrated state.<sup>30</sup> The analysis of the network structure using modern optical methods complements studies without any tracers *e.g.* scattering experiments.

Small angle neutron scattering (SANS) uses neutron scattering to probe samples on small length scales. Depending on the probed *Q*-range and the sample dimensions different structural features of an object can be studied. This is especially useful for the study of microgel particles. By choosing larger *Q*-values it becomes possible to probe properties of the internal polymer network such as correlation length which is related to the mesh size and static inhomogeneities. On the other hand, by choosing smaller *Q*-values it becomes possible to determine the radius of the microgel particle and by fitting of the scattering length density difference between solvent and sample to gain qualitative insights about the water uptake into the polymer network.<sup>14,31</sup> A number of studies discuss the internal structure of heterogeneously crosslinked microgels.<sup>14,31–36</sup>

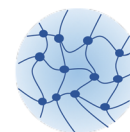
The colloidal size of the microgel particles enables the detection of the translational diffusion by dynamic light scattering, but prevents direct access to the inner dynamics. To this end, neutron scattering techniques are well-suited.

Internal dynamics in a microgel particle on a time scale between 1 ps and 1  $\mu$ s can be studied with neutron spin echo spectroscopy (NSE). This quasielastic neutron scattering technique offers a high energy resolution in the neV range. In principle, internal dynamics from cooperative network diffusion and Zimm-type dynamics, which occur on length scales below the network's mesh size, can be probed with NSE<sup>37–40</sup> and was also theoretically elucidated.<sup>41</sup> Beside quasi-elastic neutron scattering utilized by NSE also inelastic neutron scattering in combination with PFG-NMR was already used to study the inner dynamics of microgels.<sup>42</sup>

This paper focusses on the inner dynamics of PNIPAM microgel particles prepared *via* surfactant-free precipitation polymerization and a monomer feeding approach. These different synthesis routes yield the classical heterogeneously crosslinked microgels and microgels with a more homogeneous



Heterogeneous



Homogeneous

Fig. 1 Schematic structure of a heterogeneously crosslinked microgel as prepared by classical precipitation polymerization and a homogeneously crosslinked microgel prepared by continuous monomer feeding.

inner structure.<sup>20,43</sup> Fig. 1 shows a schematic representation of the anticipated internal structure of both kinds of microgels (Fig. 1–4). Neutron spin echo spectroscopy was used to reveal the local influence of the microgel network structure on its inner dynamics.

For a more thorough investigation of their internal structure neutron scattering experiments were conducted. This results in a first direct comparison of structure and dynamics of both types of microgels. Additionally, a comparison of the dynamics in both types of microgel to the dynamics of a semidilute PNIPAM solution was made to determine the influence of the network structure on the segmental dynamics.

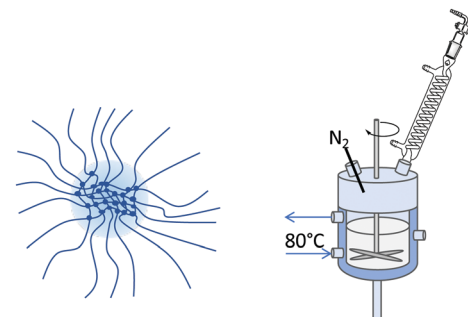


Fig. 2 Setup for the classical precipitation polymerization yielding heterogeneously crosslinked microgel particles. The different reactivities of monomer and crosslinker lead to the high density in the core region and the formation of a fuzzy outer region in the swollen state.

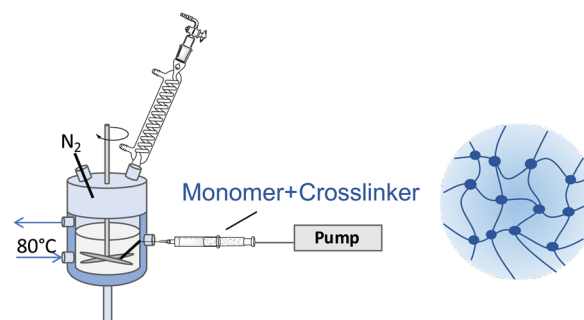


Fig. 3 Setup for the continuous monomer feeding approach yielding homogeneously crosslinked microgel particles. This approach compensates the different reactivities of monomer and crosslinker which leads to a homogeneous distribution of crosslinks in the microgel.



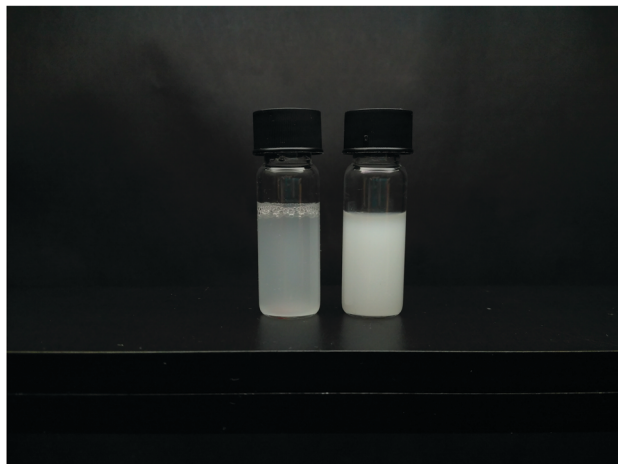


Fig. 4 Comparison between the homogeneously (MG<sub>10</sub>F) (left) and heterogeneously (MG<sub>10</sub>P) (right) crosslinked microgel particles in suspensions with  $c_{MG} = 0.5$  wt%. The structural heterogeneity of MG<sub>10</sub>P is clearly visible as a difference between the turbidity of both samples due to stronger multiple light scattering in sample MG<sub>10</sub>P.<sup>20</sup>

## 2 Experimental

### 2.1 Materials

*N*-Isopropylacrylamide (NIPAM;  $\geq 99\%$ ), poly(*N*-isopropylacrylamide) (PNIPAM; average  $M_n = 30\,000$ , PDI = 1.5), *N,N'*-methylene-bisacrylamide (BIS; 99%) and 2,2'-azobis(2-methylpropionamidine)-dihydrochloride (AAPH; 97%) were purchased from Sigma-Aldrich and used as received. D<sub>2</sub>O (99.9%) was purchased from Deutero. Water was purified with a MilliQ system (Millipore) with a resistance of 18 M $\Omega$ .

### 2.2 Microgel preparation

Heterogeneously crosslinked microgels were prepared *via* surfactant-free precipitation polymerization.<sup>44</sup> 1.527 g NIPAM and 0.232 g BIS (10 mol%) were dissolved in 120 mL water in a 250 mL double walled glass reactor with a PTFE baffle. Under continuous stirring with a PTFE stirrer at 300 rpm, the reaction solution was heated to 80 °C and purged with nitrogen for 60 min for oxygen removal. Afterwards, the stirrer was set to 1000 rpm and 68.7 mg AAPH, dissolved in 1 mL water, was added to initiate the polymerization. After 10 min the turbid microgel dispersion was released into an ice-cooled beaker to quench the reaction.

Homogeneously crosslinked microgels were prepared *via* a continuous monomer feeding approach.<sup>19,20,43</sup> 100 mL water was filled into a double walled glass reactor and treated as described above. In a separate vessel above mentioned amounts NIPAM and BIS were dissolved in 20 mL water and purged with nitrogen for 60 min. Monomer and crosslinker were filled into a syringe which was mounted onto a pump. Prior to starting the monomer feed, the initiator solution was added into the reactor and the stirrer was set to 1000 rpm. The monomer solution was fed into the reactor at a speed of 2 mL min<sup>-1</sup>. After 11 min 20 s the reaction was quenched.

To remove unreacted monomer and low molecular weight oligomers the microgel dispersion was dialyzed for 21 days with

two solvent (MilliQ water) exchanges per day. The pore size of the dialysis membrane was 14 kDa. Afterwards, the microgel dispersion was freeze-dried at -85 °C and  $1 \times 10^{-3}$  bar.

For readability the microgel with 10 mol% BIS prepared by surfactant free precipitation polymerization is referred to as MG<sub>10</sub>P and the microgel with 10 mol% BIS prepared by a continuous monomer feeding approach as MG<sub>10</sub>F in this article.

### 2.3 Viscosity measurements

Concentration-dependent viscosity measurements in D<sub>2</sub>O were carried out with a Lauda iVisc glass capillary viscometer in a temperature bath. More precisely micro-Ostwald-viscometers (type I and Ic) suited for different viscosity ranges were used to determine the efflux time  $t$  which is directly proportional to the kinematic viscosity  $\nu$  according to  $\nu = K \cdot t$ , where  $K$  is a calibration factor specific to the viscometer. The kinematic viscosity was then transformed into the dynamic viscosity  $\eta$  according to  $\eta = \nu \cdot \rho$ . For temperature equilibration the samples sat in the temperature bath for 10 minutes prior to the measurement. Each viscosity was calculated from a total of five measurements. For the conversion of the kinematic into the dynamic viscosity, the densities of each polymer solution at a given temperature were determined with an Anton Paar DMA 4500 density meter.

### 2.4 Atomic force microscopy

Atomic force microscopy (AFM) images under ambient conditions were recorded with an Asylum Research Cypher AFM (Oxford Instruments, Abington-on-Thames, UK). Imaging was done in the AC mode using an OMCL-AC240TS-R2 cantilever (Olympus) with a spring constant of  $k = 2$  N m<sup>-1</sup>. Due to the low spring constant these cantilevers are well-suited for the scanning of soft samples. To obtain single particles on the surface, cleaned silicon wafers were dipped into a highly dilute microgel dispersion and were let dry before imaging. Cross sections were analyzed with the Igor Pro software.

For the determination of the elastic properties AFM nano-indentation measurements were performed on a MFP-3D AFM (Oxford Instruments, Abington-on-Thames, UK) situated in an acoustic enclosure. At least ten individual force curves of different microgel particles were recorded for every sample at 20 °C and 50 °C. Every force curve was recorded by indenting a CSC-38-A cantilever (Mikromasch) with a spring constant of  $k = 0.2$  N m<sup>-1</sup> and a tip radius of  $R_{tip} = 8$  nm into the center of an individual microgel particle. It is important to probe in the middle of the particles, since they show a lateral stiffness gradient.<sup>45</sup> The approach part of the force curves (as shown in Fig. S5, ESI<sup>†</sup>) was fitted with the Hertz model for spherical indenters.<sup>46</sup>

$$F = \frac{4E\sqrt{R}}{3(1-\nu^2)}\delta^{3/2} \quad (1)$$

This model links the elastic modulus  $E$  of a sample with a Poisson ratio  $\nu$  with the indentation depth  $\delta$  and force  $F$  exerted by a spherical indenter of radius  $R$ . Examples for these fits are shown in the insets in Fig. S5 (ESI<sup>†</sup>). 20% of the maximum



indentation was chosen as the upper fit limit to avoid a contribution of the underlying hard substrate to the deformation of the cantilever.<sup>47–49</sup>

## 2.5 Dynamic light scattering

Temperature-dependent dynamic light scattering (DLS) measurements were performed with an ALV/CGS-3 compact goniometer (ALV GmbH, Langen, Germany). Toluene was used as a temperature and refractive index matching bath. The temperature was varied between 18 and 50 °C using a Huber thermostat. The scattering angle was varied between 30 and 100° in steps of 5° at each temperature. H<sub>2</sub>O was used as a solvent.

The setup is equipped with a He–Ne laser ( $\lambda = 632.8$  nm) with a laser intensity of 35 mW. The acquired raw data was fitted with a second-order cumulant fit in a Python based program (Python Software Foundation, Version 2.7).

## 2.6 Small angle neutron scattering

Small angle neutron scattering (SANS) experiments were performed on the KWS-2 and KWS-3 instruments of the Jülich Center for Neutron Science (JCNS) at the Heinz Maier-Leibnitz Zentrum (MLZ) (Garching, Germany). KWS-3 measurements covered a  $Q$ -range between  $3 \times 10^{-4} \text{ \AA}^{-1}$  and  $2.4 \times 10^{-3} \text{ \AA}^{-1}$  and a sample-to-detector distance of 9.5 m was chosen. The instrument KWS-2 covers a  $Q$ -range between  $1 \times 10^{-4} \text{ \AA}^{-1}$  and  $0.5 \text{ \AA}^{-1}$  at sample-to-detector distances of 2, 8 and 20 m. Thus it is suitable for studies of smaller length scales such as the study of the correlation lengths  $\xi$  in differently crosslinked microgel particles. For all SANS measurements Hellma quartz cells with a neutron path way of 2 mm were used. For linear PNIPAM chains a concentration of  $c_{\text{PNIPAM}} = 0.05 \text{ g mL}^{-1}$  and for the microgel particles of  $c_{\text{MG}} = 0.001 \text{ g mL}^{-1}$  were chosen. To ensure that the concentration of the linear PNIPAM solution was in the semidilute regime, concentration dependent viscosity measurements were carried out. For bulk contrast D<sub>2</sub>O was used as solvent.

The data was fitted using SasView (Version 2.2.0) and Igor Pro (WaveMetrics, Version 6.37).

## 2.7 Neutron spin echo spectroscopy

Neutron spin echo spectroscopy (NSE) experiments were conducted at the SNS-NSE instrument (BL-15) at the spallation neutron source (SNS, Oak Ridge, TN, USA)<sup>50</sup> and at the J-NSE instrument (MLZ, Garching, Germany).<sup>51</sup> All measurements were carried-out in transmission geometry. At the SNS-NSE two neutron wavelengths (8 and 11 Å) were combined to cover a wide range of Fourier times  $\tau$  ( $0.04 \text{ ns} \leq \tau \leq 95 \text{ ns}$ ) in a  $Q$ -range between  $0.05 \text{ \AA}^{-1}$  and  $0.20 \text{ \AA}^{-1}$ . The neutron path way in the Hellma quartz cells was 3 mm. A concentration of  $c_{\text{MG}} = 8 \text{ wt\%}$  microgel was chosen to suppress center of mass diffusion. For bulk contrast D<sub>2</sub>O was used as solvent.

Linear PNIPAM chains were measured at 15 °C at a concentration of  $c_{\text{PNIPAM}} = 0.05 \text{ g mL}^{-1}$ , which is in the semidilute concentration regime.

All microgel samples were measured at 20 °C to ensure the swollen state.

# 3 Theoretical background

## 3.1 SANS on linear polymers and microgels

SANS is an elastic scattering technique that can be used to study the structural features of polymers and microgel particles. The scattered intensity  $I(Q)$  is measured as a function of the scattering vector  $Q$  yielding characteristic scattering curves. The magnitude of the scattering vector  $Q$  is related to the scattering angle by<sup>52</sup>

$$|Q| = Q = \frac{4\pi}{\lambda} \sin\left(\frac{\theta}{2}\right) \quad (2)$$

The probed length scale  $d$  depends on the  $Q$ -range under investigation and is described by<sup>53</sup>

$$d \approx \frac{2\pi}{Q} \quad (3)$$

The equation for the scattering intensity of spherically symmetric identical particles is given by

$$I(Q) = \Delta\rho \frac{N}{V} S(Q) P(Q) + I_{\text{inc}} \quad (4)$$

Here the coherent scattering is the product of the scattering length density difference  $\Delta\rho$  between the sample and the solvent, the number of scatterers  $N$ , the structure factor  $S(Q)$  and the form factor  $P(Q)$ . As the value for  $S(Q)$  depends on interactions between particles, it can be neglected for highly dilute samples ( $S(Q) = 1$ ).  $I_{\text{inc}}$  describes the incoherent scattering due to the background.

**Microgels.** The scattered intensity of a dilute sample ( $S(Q) = 1$ ) consists of different contributions.

$$I(Q) = I_{\text{part}} + I_{\text{fluct}} + I_{\text{Porod}} + I_{\text{inc}} \quad (5)$$

$I_{\text{part}}$  describes the contribution of the overall particle shape and  $I_{\text{fluct}}$  the contribution of network fluctuations. Depending on the investigated  $Q$ -range and particle size those contributions occur in the scattering intensity distribution. At high temperatures above the VPTT the Porod law has to be applied which takes into account the local surface roughness. In this study we focus on the swollen state below the VPTT.

For  $I_{\text{part}}$  a fuzzy sphere model was used for fitting as described by Stieger *et al.* This model takes into consideration the above mentioned uneven distribution of crosslinks within the microgel particle as follows

$$I_{\text{part}}(Q) \approx P_{\text{part}}(Q) = \frac{N}{V} (\Delta\rho)^2 \left[ \frac{3[\sin(QR) - QR\cos(QR)]}{(QR)^3} \cdot \exp\left(-\frac{(\sigma_s Q)^2}{2}\right) \right]^2 \quad (6)$$

where  $\frac{N}{V}$  describes the specific surface area of the sample,  $\Delta\rho$  the difference of the scattering length densities of the microgel and the solvent ( $\rho_{\text{D}_2\text{O}} = 6.34 \times 10^{-6} \text{ \AA}^{-2}$ ) and  $R$  the radius of the sphere. A thorough display of this model can be found in ref. 14.





This model accounts for the particle surface's fuzziness by convoluting the radial box profile of the sphere model with a Gaussian.  $\sigma_s$  is the width of the smeared particle surface, often referred to as the fuzziness of the particle. The overall radius as determined by SANS is  $R_{\text{SANS}} = R + 2\sigma_s$ . The radius of the core is described by the box profile  $R_{\text{box}} = R - 2\sigma_s$ .<sup>14</sup>

At larger  $Q$  values the scattering curve can be described by a power law  $\sim Q^{-n}$ . For collapsed microgel particles an exponent of  $n \approx -4$  is observed, which corresponds to a Porod profile. However, at lower temperatures the swollen gels can be fitted with a power law with an exponent  $n \leq 4$ .

A characteristic length in microgel networks is the correlation length  $\xi$ , which describes the decay of liquid-like correlations in the polymer network. While  $\xi$  is smaller than the mean distance between the chemical crosslinks, it is proportional to it. It can be described by the Ornstein–Zernike equation

$$I_{\text{fluct}} = \frac{I_L(0)}{1 + (Q\xi)^2} \quad (7)$$

with  $I_L(0)$  being the scattered intensity at  $Q = 0$ .

**Semidilute PNIPAM solution.** In semidilute polymer solutions the scattering signal is caused by concentration fluctuations. For ideal chains the scattered intensity is well described by the Ornstein–Zernike eqn (7). In case of a polymer dissolved in a good solvent, however, the polymer coils are swollen on length scales smaller than  $\xi$  and the exponent in eqn (7) becomes the swollen fractal dimension  $D = 1/\nu \cong 1.7$ .<sup>54</sup> Since water is considered a good solvent for PNIPAM below the LCST of 32 °C eqn (8) is used to fit SANS data of a semidilute PNIPAM solution in D<sub>2</sub>O. Furthermore, we introduce a power law model  $A/Q^n$  into the fit equation. Hore *et al.* applied this law to the low- $Q$  data of a semidilute PNIPAM solution in 100% D<sub>2</sub>O, which describes composition fluctuations in the semidilute solution.<sup>55</sup> Therefore the SANS data of linear PNIPAM chains presented in this paper were fitted according to

$$I(Q) = \frac{A}{Q^n} + \frac{C}{1 + (Q\xi)^{1.7}} + I_{\text{inc}} \quad (8)$$

### 3.2 Internal dynamics from NSE on microgels

For experiments on the dynamics in bulk systems NSE measurements are carried out in transmission geometry. During an NSE experiment intermediate scattering functions  $S(Q, \tau)/S(Q, 0)$  are measured. These consist of coherent  $I_{\text{coh}}(Q, \tau)$  and incoherent  $I_{\text{inc}}(Q, \tau)$  scattering fractions. The coherently scattered neutrons have their spin up.

$$\frac{S(Q, \tau)}{S(Q, 0)} = \frac{I_{\text{coh}}(Q, \tau) - \frac{1}{3}I_{\text{inc}}(Q, \tau)}{I_{\text{coh}}(Q, \tau \approx 0) - \frac{1}{3}I_{\text{inc}}(Q, \tau \approx 0)} \quad (9)$$

This technique enables the measurement of cooperative density fluctuations of the polymer network at low  $Q$ -values and of local polymer segment dynamics for higher  $Q$ -values. In the case of semidilute polymer solutions it is expected to observe only the  $Q^3$ -dependent Zimm dynamics, since there is

no crosslinking resulting in cooperative motions of a polymer network. Long range concentration fluctuations and cooperative diffusion in the semidilute regime appear in a shorter  $Q$ -range and are rather accessible by DLS<sup>56</sup> and fluorescence correlation spectroscopy.<sup>57</sup> For microgels on the other hand the observation of cooperative network dynamics of the network breathing, similar to hydrogels,<sup>58–60</sup> is expected ( $Q^2$ -dependent) on larger length scales with a crossover to local segment dynamics ( $Q^3$ -dependent) on shorter length scales.

**Cooperative network dynamics.** In cases where only cooperative density fluctuations of the polymer network is observed, the normalized ISFs can be fitted with a single exponential decay according to

$$\frac{S(Q, \tau)}{S(Q, 0)} = \exp(-\Gamma_{\text{coop}}\tau) \quad (10)$$

where  $\Gamma_{\text{coop}}$  is the relaxation rate of the cooperative network motions and  $\tau$  the Fourier time. From  $\Gamma_{\text{coop}}$  one can calculate the cooperative diffusion coefficient  $D_{\text{coop}}$ .

$$D_{\text{coop}} = \frac{\Gamma_{\text{coop}}}{Q^2} \quad (11)$$

For purely cooperative network dynamics a display of  $D_{\text{coop}}$  against  $Q$  should result in a constant value.

From the cooperative diffusion coefficient a dynamic correlation length  $\xi_{\text{coop}}$  can be calculated from a Stokes–Einstein type relation<sup>61</sup>

$$\xi_{\text{coop}} = \frac{k_B T}{6\pi\eta D_{\text{coop}}} \quad (12)$$

**Zimm dynamics.** The Zimm model of polymer chain dynamics can be described as an extended Rouse model, which describes the segmental chain dynamics taking into consideration the hydrodynamic interactions between the chain segments. Zimm dynamics are likely observable at higher  $Q$ -values which probe local length scales on which hydrodynamic interactions become more important. In the  $Q$ -range where  $D_{\text{coop}}$  deviates from a constant value the normalized ISFs are therefore fitted with a single stretched exponential decay according to

$$\frac{S(Q, \tau)}{S(Q, 0)} = \exp(-\Gamma_{\text{Zimm}}\tau)^\beta \quad (13)$$

with  $\Gamma_{\text{Zimm}}$  the relaxation rate of the Zimm dynamics,  $\tau$  the Fourier time and  $\beta$  the exponent. A value of  $\beta = 0.85$  is typical for Zimm dynamics.<sup>62</sup> In the Zimm regime a  $Q^3$ -dependent behavior is observed. The Zimm parameter  $D_{\text{Zimm}}$  can be calculated according to

$$D_{\text{Zimm}} = \frac{\Gamma_{\text{Zimm}}}{Q^3} \quad (14)$$

To obtain an apparent solvent viscosity eqn (15) can be used.

$$\eta_{\text{app}} = \frac{k_B T}{6\pi D_{\text{Zimm}}} \frac{1}{1.354} \quad (15)$$

For better comparability the apparent viscosity can be transformed into the specific viscosity. The specific viscosity is a



dimensionless number that measures the contribution of a polymer to the solution viscosity and allows a direct comparison between different samples. It is defined as

$$\eta_{sp} = \frac{\eta_{app} - \eta_s}{\eta_s} \quad (16)$$

where  $\eta_{app}$  is the apparent viscosity from NSE measurements and  $\eta_s$  the solvent viscosity.<sup>54</sup>

## 4 Results & discussion

### 4.1 Dynamic light scattering on microgel particles

Temperature-dependent dynamic light scattering measurements were carried out to investigate the thermoresponsive properties of the microgel particles. The hydrodynamic radii,  $R_h$ , as a function of the temperature,  $T$ , are displayed in Fig. 5.

MG<sub>10</sub>P has a hydrodynamic radius of  $R_{h,swollen} = (310 \pm 2)$  nm at 20 °C (PDI = 0.06) and  $R_{h,collapsed} = (186 \pm 1)$  nm at 50 °C (PDI = 0.04). MG<sub>10</sub>F is in a similar size range with a hydrodynamic radius of  $R_{h,swollen} = (463 \pm 7)$  nm (PDI = 0.26) and  $R_{h,collapsed} = (214 \pm 2)$  nm (PDI = 0.23). This corresponds well to the common observation of low polydispersity in case of microgels synthesized *via* precipitation polymerization. In contrast to this, MG<sub>10</sub>F has a moderate size distribution in the swollen and collapsed state. The different sizes in the collapsed state might result from different amounts of incorporated crosslinker and monomer, which limits a quantitative comparison of the swelling ratios ( $\alpha_{DLS} = R_{h,20^\circ C}/R_{h,50^\circ C}$ ,  $\alpha_{DLS,MG10P} = 1.67$ ,  $\alpha_{DLS,MG10F} = 2.16$ ). Hence, the difference in the swelling ratios cannot be exclusively attributed to the different inner structures of both microgels.

### 4.2 Atomic force microscopy

Fig. 6 shows the height profiles of (a) an individual MG<sub>10</sub>P microgel particle and (b) an individual MG<sub>10</sub>F microgel particle in the dry state with corresponding cross sections. From the cross sections the height-to-lateral width ratio was determined

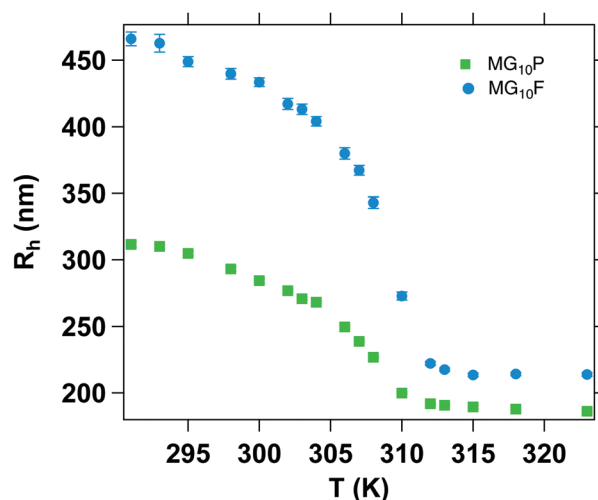


Fig. 5 Temperature-dependent hydrodynamic radii of MG<sub>10</sub>P and MG<sub>10</sub>F.

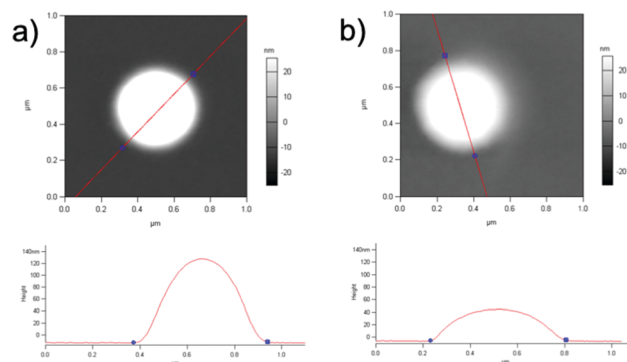


Fig. 6 AFM height images of (a) a MG<sub>10</sub>P microgel particle and (b) a MG<sub>10</sub>F microgel particle in the dry state with corresponding cross section (height profile, red line).

to be 0.25 for MG<sub>10</sub>P and 0.08 for MG<sub>10</sub>F. This illustrates the lower deformation of MG<sub>10</sub>P in the adsorbed state perpendicular to the substrate. This results from the presence of a densely crosslinked core region. For the microgels resulting from a continuous monomer feeding approach we observe higher deformation, which suggests a more homogeneous distribution of the crosslinks. Due to the high crosslinker content the typical fried egg type structure is not as visible.<sup>63</sup>

The lateral dimensions of the microgels in Fig. 6 are similar. Hence, the difference between the heights can most likely be attributed to the difference in the mechanical properties of the microgels and MG<sub>10</sub>P appears stiffer and more resistant against vertical deformation in the adsorbed state.

In Fig. S5 in the ESI† for both types of microgels a set of force-distance curves is shown for the swollen and the collapsed state. When the tip is in contact with the adsorbed microgel, the force rises at increasing indentation. When indenting into the MG<sub>10</sub>P and the MG<sub>10</sub>F sample to the same depth the required force is larger for MG<sub>10</sub>P than for MG<sub>10</sub>F. This indicates a softer material of MG<sub>10</sub>F which agrees to the smaller measured height of MG<sub>10</sub>F in the dry adsorbed state. In the collapsed state at 50 °C the difference between the force curves reduces and the indentation at a given force reduces compared to the swollen state. All force-distance curves show a steady progression which indicates the absence of discontinuities of the mechanical properties as recently reported for a comparison of the mechanics of adsorbed core-shell and hollow microgels.<sup>64</sup> The averaged data was fitted with the Hertz model for spherical indenters as described in Section 2.4. Table 1 summarizes the resulting Young's moduli of both microgel systems in the swollen and collapsed state. The results show that the Young's modulus of MG<sub>10</sub>P is almost twice the Young's modulus of MG<sub>10</sub>F in the swollen state. Therefore, the network appears stiffer, which can be explained by the formation of a denser core during classical precipitation polymerization. In the collapsed state the Young's modulus for both microgel systems is the same within the error range. This can be explained with the repulsion of water molecules from the polymer network, which changes the internal structure of the microgel particles. The Young's moduli have the same order of magnitude as previously reported data from neutral PNIPAM



**Table 1** Young's moduli  $E$  of MG<sub>10</sub>P and MG<sub>10</sub>F measured via AFM at 20 °C in the swollen and at 50 °C in the collapsed state

Microgel	$E_{20^\circ\text{C}}$ [kPa]	$E_{50^\circ\text{C}}$ [kPa]
MG <sub>10</sub> P	$312 \pm 38$	$1004 \pm 67$
MG <sub>10</sub> F	$166 \pm 24$	$1070 \pm 106$

microgels of somewhat lower crosslinker content<sup>45</sup> and copolymerized ionic PNIPAM microgels.<sup>65</sup> They also agree well to the observation of rather small Young's moduli previously reported for much softer PNIPAM microgels with 0.25% BIS corresponding the predictions from scaling theory of polymer gels in good solvents.<sup>66</sup>

### 4.3 SANS of a semidilute solution of linear PNIPAM chains

SANS measurements of a semidilute solution of linear PNIPAM chains were carried out in a  $Q$ -range of  $2 \times 10^{-3}$ – $0.4 \text{ \AA}^{-1}$ . The data were fitted according to eqn (8). As a comparison a simple Ornstein–Zernike fit was carried out as well as is displayed in Fig. 7. This however does not sufficiently describe the curve for  $Q$ -values below  $2 \times 10^{-2} \text{ \AA}^{-1}$  where composition fluctuations dominate the scattering signal. A comparison of the results for the different models can be found in the ESI.†

A fit according to eqn (8) yields a correlation length of  $\xi = (2.40 \pm 0.02) \text{ nm}$  with the power law exponent  $n = 1.2 \pm 0.01$ . Meier-Koll *et al.* investigated PNIPAM chains with a molecular weight of  $25\,000 \text{ g mol}^{-1}$  and a concentration of 13 wt% and found values for the correlation length below 2 nm at 15 °C. Therefore our value of 2.4 nm at a lower polymer concentration of 4.5 wt% (corresponding to  $0.05 \text{ g mL}^{-1}$ ) and a slightly higher molecular number of  $30\,000 \text{ g mol}^{-1}$  appears reasonable.<sup>67</sup>

### 4.4 SANS of highly crosslinked PNIPAM microgels

SANS curves of MG<sub>10</sub>P and MG<sub>10</sub>F measured at 20 °C at identical experimental conditions are displayed in Fig. 8. The inset shows

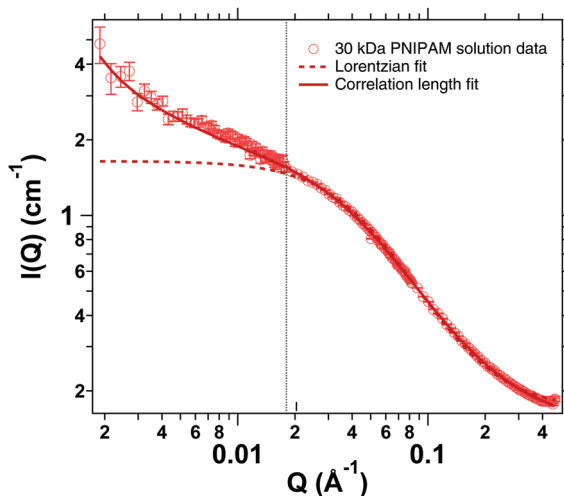


**Fig. 7** SANS measurements of a semidilute solution of linear PNIPAM chains for higher  $Q$ -values. Comparison between a simple Lorentzian (dashed) and a correlation length fit model (solid).

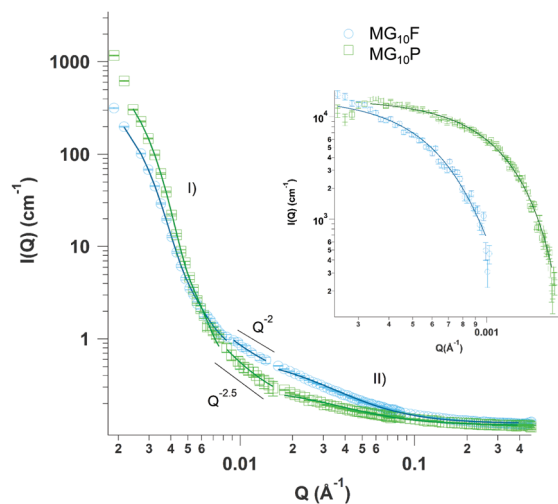


**Fig. 8** SANS curves for MG<sub>10</sub>P and MG<sub>10</sub>F at higher  $Q$ -values measured on KWS-2. (I) Fuzzy sphere model,<sup>14</sup> (II) Ornstein–Zernike fit. In the intermediate range between (I) and (II) the scattered intensity changes according to a power law. The inset shows the scattering curves at lower  $Q$ -values as measured on KWS-3 and fitted with a Fuzzy sphere model.

the scattering curves at small  $Q$ -values ( $2.3 \times 10^{-4} \text{ \AA}^{-1} \leq Q \leq 1.9 \times 10^{-3} \text{ \AA}^{-1}$ ). Here larger length scales are probed and information on the overall radii of the microgel particles is obtained. A fit according to eqn (6) yields  $R_{\text{MG10P}} = (200.0 \pm 0.4) \text{ nm}$  and  $R_{\text{MG10F}} = (288.7 \pm 1.7) \text{ nm}$ . These values are in good agreement to the radii of gyration  $R_g$  obtained from a Guinier analysis which yields  $R_g = (176 \pm 1) \text{ nm}$  for MG<sub>10</sub>P and  $R_g = (307 \pm 2) \text{ nm}$  for MG<sub>10</sub>F. The comparison to the hydrodynamic radii in the swollen state gives  $R_g/R_h = 0.57$  for MG<sub>10</sub>P and  $R_g/R_h = 0.66$  for MG<sub>10</sub>F. Compared to the theoretical ratio of 0.78 for hard spheres, both values indicate the soft nature of the microgels (Table 2).

In Fig. 8 the scattering curve is subdivided into two distinct fitting areas denoted (I) and (II). In (I) a fit according to the fuzzy sphere model (eqn (6)) was carried out to determine the fuzziness  $\sigma_s$  of the spheres. The resulting fuzziness is higher for MG<sub>10</sub>P ( $\sigma_{s,\text{MG10P}} = 17.4 \pm 0.3 \text{ nm}$ ) compared to MG<sub>10</sub>F ( $\sigma_{s,\text{MG10F}} = 4.2 \pm 0.5 \text{ nm}$ ). Taking into consideration the overall radii as determined on KWS-3 this accounts for 8.7% for Het10MG and only 1.5% for MG<sub>10</sub>F. In fit range (II) the scattering curve was fitted with an Ornstein–Zernike equation. The range in between was not perfectly fitted by the superposition of the fuzzy sphere model and the Ornstein–Zernike equation and was therefore

**Table 2** Hydrodynamic radius  $R_{h,\text{DLS}}$  determined from DLS and size parameters  $R_g$ ,  $R_{\text{SANS}}$ ,  $R_{\text{box}}$  and  $\sigma_s$  extracted from fitting the SANS data

Microgel	$R_{h,\text{DLS}}$ [nm]	$R_g$ [nm]	$R_{\text{SANS}}$ [nm]	$R_{\text{box}}$ [nm]	$\sigma_s$ [nm]
20 °C					
MG <sub>10</sub> P	$310 \pm 2$	$176 \pm 1$	235	$200 \pm 1$	$17.4 \pm 0.3$
MG <sub>10</sub> F	$463 \pm 7$	$307 \pm 2$	298	$289 \pm 2$	$4.2 \pm 0.5$
50 °C					
MG <sub>10</sub> P	$186 \pm 1$	$120 \pm 1$	138	$124 \pm 2$	$6.0 \pm 0.1$
MG <sub>10</sub> F	$214 \pm 2$	$150 \pm 1$	155	$135 \pm 2$	$0.1 \pm 1$

**Table 3** Correlation lengths from SANS according to the Ornstein-Zernike fit  $\xi_{\text{OZ-fit}}$ .  $I_L(0)$  is the scattered intensity at  $Q = 0$

Microgel	$I_L(0)$ [ $\text{cm}^{-1}$ ]	$\xi_{\text{OZ-fit}}$ [nm]
MG <sub>10</sub> P	$0.090 \pm 0.002$	$2.00 \pm 0.04$
MG <sub>10</sub> F	$0.33 \pm 0.01$	$3.21 \pm 0.05$

omitted. The scattered intensity in this region varies according to a power law  $I \propto Q^{-m}$ . Exponents of  $-2.5$  and  $-2$  for MG<sub>10</sub>P and MG<sub>10</sub>F are found respectively. The Ornstein-Zernike fit yields the average correlation length  $\xi_{\text{OZ-fit}}$ . For MG<sub>10</sub>P we find  $\xi_{\text{OZ-fit}} = (2.00 \pm 0.04)$  nm and  $\xi_{\text{OZ-fit}} = (3.21 \pm 0.05)$  nm for MG<sub>10</sub>F. The two fits show major differences in the value for  $I_L(0)$ . While MG<sub>10</sub>P has a value of  $I_L(0) = (0.090 \pm 0.002) \text{ cm}^{-1}$ , the value for MG<sub>10</sub>F is much higher with  $I_L(0) = (0.33 \pm 0.01) \text{ cm}^{-1}$ . Karg *et al.* found when analyzing the internal particle morphology of heterogeneously crosslinked microgel particles with different amounts of crosslinker (2, 5 and 10% BIS) that  $I_L(0)$  decreases with increasing connectivity of the network.<sup>32</sup> Therefore the findings show a higher contribution of the fluid like thermal fluctuations to the scattering signal of MG<sub>10</sub>F. An overview of the resulting fit parameters can be found in Table 3.

The SANS data of the collapsed state at  $50^\circ\text{C}$  are shown in the ESI† in Fig. S6. In the medium- and high- $Q$  range the data can be fitted with a Porod decay  $I(Q) \propto Q^{-4}$ . Fits with the fuzzy sphere model in the low- $Q$  range result in  $R_{\text{SANS}} = (138 \pm 4)$  nm for MG<sub>10</sub>P and  $R_{\text{SANS}} = (155 \pm 1)$  nm for MG<sub>10</sub>F. The corresponding values of  $R_g$  are  $R_g = (120 \pm 2)$  nm and  $R_g = (150 \pm 5)$  nm for MG<sub>10</sub>P and MG<sub>10</sub>F. For the collapsed state  $R_g/R_h = 0.65$  for MG<sub>10</sub>P and  $R_g/R_h = 0.70$  for MG<sub>10</sub>F were obtained. This suggests a decreasing polymer density towards the exterior. So far, the conclusion can be drawn, that in the feeding approach the structural heterogeneity is strongly reduced but remains most probably in the periphery of the particles.

#### 4.5 Internal dynamics from NSE

**Cooperative network dynamics.** Normalized ISFs were first fitted according to eqn (10) and the resulting values for the cooperative diffusion coefficient  $D_{\text{coop}}$  were calculated according to eqn (14). In Fig. 9  $D_{\text{coop}} = \Gamma/Q^2$  is displayed over  $Q$ . As described above  $D_{\text{coop}}$  will be a constant value, if only cooperative network dynamics are observed over the entire  $Q$ -range. In this case  $D_{\text{coop}}$  can be extracted from a linear fit of  $\Gamma/Q^2$  vs.  $Q$  with a slope of zero.

Fig. 9 clearly shows differences among the three investigated samples. For MG<sub>10</sub>P  $D_{\text{coop}}$  display a constant value over the entire  $Q$ -range. However, for MG<sub>10</sub>F there is a transition from a constant value to an increase at around  $0.11 \text{ \AA}^{-1}$ . Therefore, it appears that the cooperative network dynamics dominate at lower  $Q$ -values, but that Zimm dynamics become observable at higher  $Q$ -values. We assume a superposition of both types of dynamics with a gradual change of their amplitudes at increasing  $Q$ -values.  $D_{\text{coop}}$  of MG<sub>10</sub>F was therefore calculated from a linear fit with a slope of zero of the three lowest  $Q$ -values in Fig. 9. As might be expected the semidilute linear PNIPAM solution displays a deviation from a constant value over the entire  $Q$ -range,

since single chain dynamics are observed due to a lack of a crosslinked polymer network. Therefore, NSE data of the semidilute PNIPAM solution was fitted according to eqn (13) with  $\beta = 0.85$ .

We observe that many of the normalized ISFs don't decay to zero. This means that there are elastic contributions to the scattering signal which *e.g.* hints at the existence of inhomogeneities within the polymer network with very slow to no dynamics. Therefore, the fitting eqn (10) and (13) were extended by an additional term  $(1 - A)$  accounting for the elastic contribution (eqn (17)). The values for  $(1 - A)$  for both microgels are shown in Tables 5 and 6. As  $Q$  increases and hence the observed length scale decreases, the elastic contribution decreases. For the sample MG<sub>10</sub>F, the elastic contribution vanishes completely at those  $Q$ -values corresponding to the Zimm regime. Scherzinger *et al.* found similar values for the elastic contribution in PDEAAM-core-PNIPAM-shell particles.<sup>38</sup>

$$\frac{S(Q, \tau)}{S(Q, 0)} = (1 - A) + A \cdot \exp(-\Gamma\tau) \quad (17)$$

Table 4 lists the cooperative diffusion coefficients for the investigated samples. For the sample prepared by precipitation polymerization the value of  $D_{\text{coop}} = (2.69 \pm 0.02) \times 10^{-11} \text{ m}^2 \text{ s}^{-1}$  is in agreement with data published by Hellweg *et al.*,<sup>68</sup> who also investigated dynamics of PNIPAM microgel particles with different amounts of crosslinker. For the microgel prepared by a continuous monomer feeding approach the cooperative

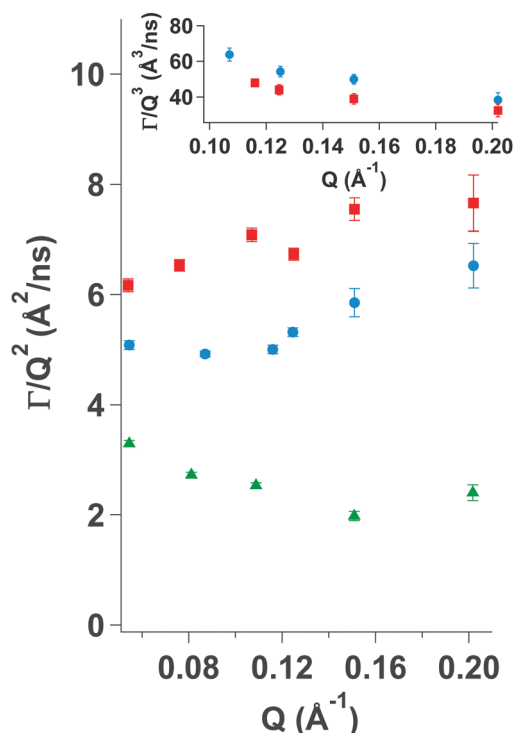


**Fig. 9** Diffusion coefficient  $D_{\text{col}} = \Gamma/Q^2$  against  $Q$ . While MG<sub>10</sub>P (green triangles) shows a constant value over the entire  $Q$ -range, and the linear PNIPAM solution (red squares) shows a continuous increase, MG<sub>10</sub>F (blue circles) has a constant value up to  $Q = 0.11 \text{ \AA}^{-1}$  and increases afterwards.





**Table 4** Results of the NSE measurements. Summarized are the cooperative diffusion coefficient  $D_{\text{coop}}$  and the dynamic correlation length  $\xi_{\text{coop}}$ 

Sample	$T$ [°C]	$D_{\text{coop}}$ [ $10^{-11} \text{ m}^2 \text{ s}^{-1}$ ]	$\xi_{\text{coop}}$ [nm]
MG <sub>10</sub> P	20	$2.69 \pm 0.02$	6.4
MG <sub>10</sub> F	20	$4.98 \pm 0.04$	3.4

**Table 5** Elastic contribution  $(1 - A)$  to the ISFs of MG<sub>10</sub>P.  $\Delta(1 - A)$  is the error as determined by a fit according to eqn (17)

$Q$ ( $\text{\AA}^{-1}$ )	$(1 - A)$	$\Delta(1 - A)$
0.05	0.45907	0.0519
0.08	0.37785	0.0301
0.11	0.32318	0.0169
0.15	0.27728	0.0187
0.20	0.20948	0.0439

diffusion coefficient is approximately twice the value of MG<sub>10</sub>P. This indicates a faster decay of the network fluctuations and thus a less stiff network. This is in agreement with the AFM measurements of Young's moduli on adsorbed microgel particles presented in Section 4.2.

Using  $\eta_{\text{D}_2\text{O}} = 1.251 \text{ cP}$  at  $T = 20^\circ \text{C}$  eqn (12) yields values of  $\xi_{\text{coop}} = 6.4 \text{ nm}$  for MG<sub>10</sub>P and  $\xi_{\text{coop}} = 3.4 \text{ nm}$  for MG<sub>10</sub>F. This indicates that cooperative network fluctuations in sample MG<sub>10</sub>P have larger decay lengths. This suggests, that the polymer network of sample MG<sub>10</sub>F is softer in the size range explored by NSE due to the absence of a dense inner core region. A comparison with data published by Hellweg *et al.* shows that the dynamics of MG<sub>10</sub>F behave similar to a microgel prepared *via* precipitation polymerization with a low crosslinker content.<sup>68</sup>

Generally, the collective diffusion coefficient  $D_{\text{coop}} = E/f$  relates an elastic modulus to the friction coefficient  $f$  which considers the resistance against the relative motion of polymer network and solvent. It measures the relaxation of concentration fluctuations in the network. The elastic modulus of a gel  $E = K + 4/3G$  is determined by the osmotic bulk modulus  $K$  describing network deformations including volume changes and the shear modulus  $G$  accounting for deformations without a volume change.

In previous mechanical measurements of the friction coefficient in macroscopic poly(acrylamide) hydrogels using confocal laser scanning microscopy a decrease of  $f$  with increasing crosslinker content and the accompanying increase of structural heterogeneities was observed.<sup>69–71</sup> It was argued that the motion in regions of low crosslinker density contributes more

**Table 6** Elastic contribution  $(1 - A)$  to the ISFs of the MG<sub>10</sub>F.  $\Delta(1 - A)$  is the error as determined by a fit according to eqn (17). Note, the elastic contribution virtually vanishes at large  $Q$  values compared to  $A$  at the same  $Q$  values in Table 5

$Q$ ( $\text{\AA}^{-1}$ )	$(1 - A)$	$\Delta(1 - A)$
0.05	0.410963	0.0212
0.08	0.253	0.0146
0.11	0.10076	0.0111
0.15	−0.035338	0.0225
0.20	−0.026817	0.0266

**Table 7** Results of the NSE measurements. Summarized are the Zimm parameter  $D_{\text{Zimm}}$  and the effective and specific viscosity  $\eta_{\text{app}}$  and  $\eta_{\text{sp}}$ . The differences for  $\eta_{\text{sp}}$  occur due to the different temperature during the measurement

Sample	$T$ [°C]	$D_{\text{Zimm}}$ [ $\text{\AA}^3 \text{ ns}^{-1}$ ]	$\eta_{\text{app}}$ [cP]	$\eta_{\text{sp}}$ [cP]
MG <sub>10</sub> P	20	—	—	—
MG <sub>10</sub> F	20	$42.5 \pm 1.5$	3.7	1.96
PNIPAM solution	15	$49.2 \pm 1.8$	3.2	1.22

to the friction coefficient than the motion in the region of higher polymer and crosslinking density.

In heterogeneously crosslinked microgel particles the size of the dense core region with its higher polymer and crosslinker density increases with increasing crosslinker content and hence, its contribution to the net friction coefficient of the particle increases.

**Zimm dynamics.** A linear fit with a slope of zero of  $\Gamma_{\text{Zimm}}/Q^3$  yields  $D_{\text{Zimm}}$ , from which the apparent viscosity  $\eta_{\text{app}}$  was calculated with eqn (15) for those samples displaying Zimm type dynamics (Table 7).  $\Gamma_{\text{Zimm}}/Q^3$  is displayed against  $Q$  for the semidilute PNIPAM solution and MG<sub>10</sub>F in the inset in Fig. 9. One might expect MG<sub>10</sub>P to display Zimm type dynamics from the fluffy shell. However, within the accessible  $Q$ -range this was not observed. This corresponds well to the larger dynamic correlation length  $\xi_{\text{coop}}$  of MG<sub>10</sub>P. Possibly, the increase of the crosslinker content increases the decay length of the breathing like density fluctuations and hence decreases the relative amplitude of the Zimm-dynamics and shifts its contribution to higher  $Q$ .

In Table 7 the apparent and specific viscosities are listed as well. As mentioned above the specific viscosity allows a statement about the contribution of a polymer to the solution viscosity and a comparison between the different samples. We find values of  $\eta_{\text{sp}} = 1.96$  and  $1.22$  for MG<sub>10</sub>F and the semidilute PNIPAM solution respectively. These values show that the polymer has a non-negligible contribution to the viscosity in both samples (Fig. 10).

The increased apparent viscosity may be attributed to cooperative hydration, which has been described in the literature for PNIPAM chains and microgels based on PNIPAM.<sup>72–75</sup> Due to the formation of hydrophobic isopropyl side groups, there is a positive correlation between neighboring bound water molecules, favoring the formation of further hydrogen bonds. It is assumed that the formation of these hydrogen bonds increases the local viscosity in such polymer systems.<sup>76</sup> Concentration dependent viscosity measurements of linear PNIPAM in D<sub>2</sub>O (Fig. 11) show that the specific viscosity of  $1.22$  corresponds to a PNIPAM concentration of  $35 \text{ mg mL}^{-1}$ , which is slightly below the actual concentration of  $50 \text{ mg mL}^{-1}$  chosen for the experiment.

Moreover, the analysis of the SANS data presented in Section 4.4 revealed a stronger contribution of fluid like fluctuations in case of MG<sub>10</sub>F. Possibly larger fluctuation amplitudes of the polymer segments also contribute to the increase of  $\eta_{\text{app}}$ . A similar behavior was found for microgels during NSE studies of cononsolvency effects on the dynamics of microgels.<sup>38–40</sup>



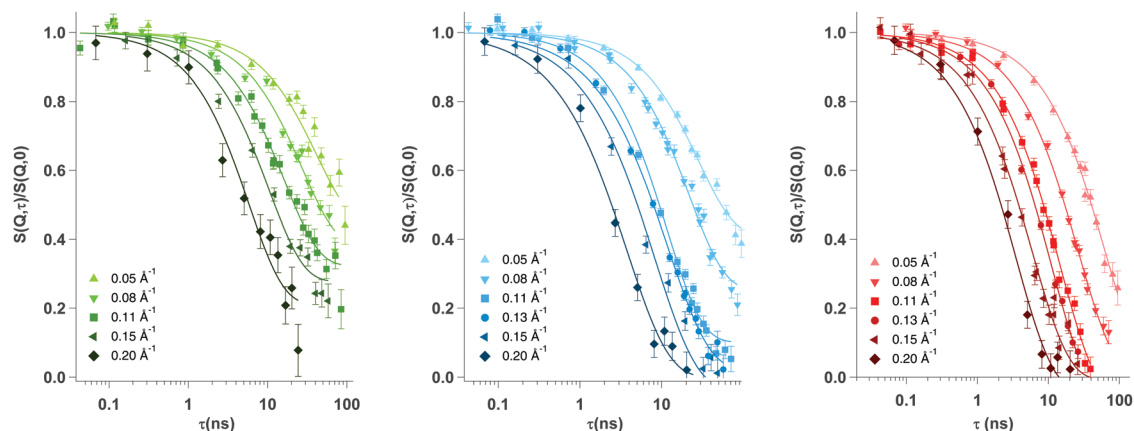


Fig. 10 Normalized ISFs of MG<sub>10</sub>P (green symbols) and MG<sub>10</sub>F (blue symbols) at 20 °C and a semidilute PNIPAM solution at 15 °C (red symbols). MG<sub>10</sub>P was fitted with eqn (17) over the entire  $Q$ -range, MG<sub>10</sub>F was fitted with eqn (17) for  $Q = 0.05, 0.08$  and  $0.11 \text{ \AA}^{-1}$  and with eqn (13) for  $Q = 0.13, 0.15$  and  $0.20 \text{ \AA}^{-1}$ . The semidilute PNIPAM solution was fitted with eqn (13).

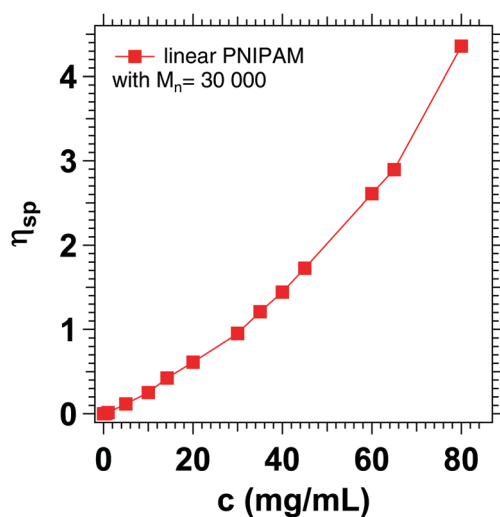


Fig. 11 Specific viscosity of linear PNIPAM with  $M_n = 30 \text{ kDa}$  at different concentrations in D<sub>2</sub>O.

Microgels are often discussed as potential carrier medium for nanoparticles, proteins or therapeutic drugs and diagnostic agents. Microgel size, cross-linking density, and network homogeneity are discussed as important influences on the loading capacity and release/uptake kinetics.<sup>77</sup> The inner dynamics of the microgel network may also influence the diffusion of probes inside the gel due to hydrodynamic friction between the polymer chains, the solvent and the probes. Therefore, it should also be considered in uptake and release scenarios.

## 5 Conclusions

Two kinds of PNIPAM based microgel particles with a high crosslinker content were prepared *via* classical precipitation polymerization (MG<sub>10</sub>P) and a continuous monomer feeding approach (MG<sub>10</sub>F). Their structure was investigated with dynamic light scattering and small angle neutron scattering, which revealed clear differences between their inner structure.

MG<sub>10</sub>P displayed a higher fuzziness ( $\sigma_s \approx 17 \text{ nm}$ ), compared to MG<sub>10</sub>F ( $\sigma_s \approx 4 \text{ nm}$ ). Furthermore, MG<sub>10</sub>F has a slightly higher correlation length  $\xi_{\text{OZ-fit}}$  than MG<sub>10</sub>P. AFM measurements of adsorbed microgels in the dry state of both systems show differences in the particle morphology and the measurement of the Young's moduli indicates a softer network in case of MG<sub>10</sub>F. Dynamics as investigated by neutron spin echo spectroscopy revealed that in MG<sub>10</sub>P the presence of a dense core region leads to a dominance of the cooperative dynamics. Zimm-type dynamics could only be observed for MG<sub>10</sub>F, while a simple  $Q^2$  dependence was observed for the dynamics in MG<sub>10</sub>P in the entire measured  $Q$ -range. This corresponds to the results of the AFM indentation measurements. As a comparison to the dynamic properties in both microgels, an aqueous semidilute PNIPAM solution was measured in the same  $Q$ -range, which as expected showed a deviation from  $Q^2$  dependence, as can be attributed to the observation of Zimm-type dynamics. Interestingly, the pure Zimm-regime was not reached for any sample in the observed  $Q$ -range. This leads to the conclusion that higher  $Q$ -values would be required to observe pure Zimm-type dynamics. A calculation of the specific viscosity resulted in values  $1.2 < \eta_{\text{sp}} < 2.0$ . Therefore, a contribution of the polymer to the apparent viscosity is observed which in the case of PNIPAM can be attributed to cooperative hydration of the polymer network, which leads to an increased viscosity. Interestingly, MG<sub>10</sub>P shows a clear elastic contribution over the entire  $Q$ -range, while MG<sub>10</sub>F only shows this contribution at very low  $Q$ -values. A comparison with NSE measurements of a lowly crosslinked PNIPAM based microgel revealed that in terms of the cooperative diffusion a high value is measured and a transition to the observation of Zimm-dynamics at a similar  $Q$ -value as for MG<sub>10</sub>F is observed. The presence of the dense inner region of a heterogeneously crosslinked microgel leads to the dominant contribution of cooperative density fluctuations to the observed dynamics.

In summary, MG<sub>10</sub>F synthesized *via* a monomer feeding method has a more homogeneous inner network structure than MG<sub>10</sub>P prepared *via* the classical precipitation polymerization



but heterogeneity is still present in the periphery of the particles. The structural differences also clearly affect the dynamic properties. The denser network of MG<sub>10</sub>P leads to a dominant cooperative dynamics while in case of MG<sub>10</sub>F also segmental dynamics contributes.

## Conflicts of interest

There are no conflicts to declare.

## Acknowledgements

The D<sub>2</sub>O used in the NSE experiments was supplied by the United States Department of Energy Office of Science by Isotope Program in the Office of Nuclear Physics. This work is based upon experiments performed at the KWS-2 and KWS-3 operated by JCNS at Heinz Maier-Leibnitz Zentrum (MLZ), Garching, Germany. We also thank Malcolm Cochran for technical support during the beam time at SNS-NSE and Piotr A. Zolnierczuk for support with NSE data analysis. S. W. and O. H. gratefully acknowledge the financial support by Deutsche Forschungsgemeinschaft DFG (grant number WE5066/3-1 (S. Wellert) and HO 5488/2-1 (O. Holderer)).

## Notes and references

- 1 D. Sivakumaran, D. Maitland and T. Hoare, *Biomacromolecules*, 2011, **12**, 4112–4120.
- 2 T. K. Bronich, S. V. Vinogradov and A. V. Kabanov, *Nano Lett.*, 2001, **1**, 535–540.
- 3 D. M. Mock, G. Lankford and P. Horowitz, *Biochim. Biophys. Acta, Protein Struct. Mol. Enzymol.*, 1988, **956**, 23–29.
- 4 L. Hu and M. J. Serpe, *Chem. Commun.*, 2013, **49**, 2649–2651.
- 5 M. R. Islam and M. J. Serpe, *Chem. Commun.*, 2013, **49**, 2646–2648.
- 6 Y. Liu, Y. Zhang and Y. Guan, *Chem. Commun.*, 2009, 1867–1869.
- 7 K. Iwai, Y. Matsumura, S. Uchiyama and A. P. de Silva, *J. Mater. Chem.*, 2005, **15**, 2796–2800.
- 8 C. M. Nolan, C. D. Reyes, J. D. Debord, A. J. Garcia and L. A. Lyon, *Biomacromolecules*, 2005, **6**, 2032–2039.
- 9 N. Singh, A. W. Bridges, A. J. Garca and L. A. Lyon, *Biomacromolecules*, 2007, **8**, 3271–3275.
- 10 A. W. Bridges, N. Singh, K. L. Burns, J. E. Babensee, L. A. Lyon and A. J. Garca, *Biomaterials*, 2008, **29**, 4605–4615.
- 11 J. D. Debord and L. A. Lyon, *Langmuir*, 2003, **19**, 7662–7664.
- 12 Y. Zhang, Y. Guan and S. Zhou, *Biomacromolecules*, 2006, **7**, 3196–3201.
- 13 X. Wu, R. Pelton, A. Hamielec, D. Woods and W. McPhee, *Colloid Polym. Sci.*, 1994, **272**, 467–477.
- 14 M. Stieger, W. Richtering, J. S. Pedersen and P. Lindner, *J. Chem. Phys.*, 2004, **120**, 6197–6206.
- 15 S. Meyer and W. Richtering, *Macromolecules*, 2005, **38**, 1517–1519.
- 16 H. J. M. Wolff, M. Kather, H. Breisig, W. Richtering, A. Rich and M. Wessling, *ACS Appl. Mater. Interfaces*, 2018, **10**, 24799–24806.
- 17 S. Seiffert, *Macromol. Rapid Commun.*, 2012, **33**, 1135–1142.
- 18 A. Habicht, W. Schmolke, F. Lange, K. Saalwächter and S. Seiffert, *Macromol. Chem. Phys.*, 2014, **215**, 1116–1133.
- 19 T. Still, K. Chen, A. M. Alsayed, K. B. Aptowicz and A. Yodh, *J. Colloid Interface Sci.*, 2013, **405**, 96–102.
- 20 R. Acciaro, T. Gilanyi and I. Varga, *Langmuir*, 2011, **27**, 7917–7925.
- 21 M. Füllbrandt, R. von Klitzing and A. Schönhals, *Soft Matter*, 2013, **9**, 4464–4471.
- 22 W. Su, K. Zhao, J. Wei and T. Ngai, *Soft Matter*, 2014, **10**, 8711–8723.
- 23 A. J. Moreno and F. Lo Verso, *Soft Matter*, 2018, **14**, 7083–7096.
- 24 F. A. Plamper and W. Richtering, *Acc. Chem. Res.*, 2017, **50**, 131–140.
- 25 P. S. Mohanty, S. Nöjd, K. van Gruijthuijsen, J. J. Crassous, M. Obiols-Rabasa, R. Schweins, A. Stradner and P. Schurtenberger, *Sci. Rep.*, 2017, **7**, 1487.
- 26 J. Mattsson, H. M. Wyss, A. Fernández-Nieves, K. Miyazaki, Z. Hu, D. R. Reichman and D. A. Weitz, *Nature*, 2009, **462**, 83.
- 27 T. Hiroi, M. Ohl, T. Sakai and M. Shibayama, *Macromolecules*, 2014, **47**, 763–770.
- 28 S. Bergmann, O. Wrede, T. Huser and T. Hellweg, *Phys. Chem. Chem. Phys.*, 2018, **20**, 5074–5083.
- 29 A. P. Gelissen, A. Oppermann, T. Caumanns, P. Hebbeker, S. K. Turnhoff, R. Tiwari, S. Eisold, U. Simon, Y. Lu and J. Mayer, *et al.*, *Nano Lett.*, 2016, **16**, 7295–7301.
- 30 E. Siemes, O. Nevskiy, D. Sysoiev, S. K. Turnhoff, A. Oppermann, T. Huhn, W. Richtering and D. Wöll, *Angew. Chem., Int. Ed.*, 2018, **57**, 12280–12284.
- 31 S. Höfl, L. Zitzler, T. Hellweg, S. Herminghaus and F. Mugele, *Polymer*, 2007, **48**, 245–254.
- 32 M. Karg, S. Prévost, A. Brandt, D. Wallacher, R. von Klitzing and T. Hellweg, *Intelligent Hydrogels*, Springer, 2013, vol. 140, pp. 63–76.
- 33 K. Kratz, T. Hellweg and W. Eimer, *Polymer*, 2001, **42**, 6631–6639.
- 34 K. Kratz, A. Lapp, W. Eimer and T. Hellweg, *Colloids Surf., A*, 2002, **197**, 55–67.
- 35 K. Kratz, A. Lapp, W. Eimer and T. Hellweg, *Colloids Surf., A*, 2002, **197**, 55–67.
- 36 Y. Hertle, M. Zeiser, P. Fouquet, M. Maccarini and T. Hellweg, *Z. Phys. Chem.*, 2014, **228**, 1053–1075.
- 37 T. Hellweg, K. Kratz, S. Pouget and W. Eimer, *Colloids Surf., A*, 2002, **202**, 223–232.
- 38 C. Scherzinger, O. Holderer, D. Richter and W. Richtering, *Phys. Chem. Chem. Phys.*, 2012, **14**, 2762–2768.
- 39 S. Maccarrone, C. Scherzinger, O. Holderer, P. Lindner, M. Sharp, W. Richtering and D. Richter, *Macromolecules*, 2014, **47**, 5982–5988.
- 40 S. Maccarrone, A. Ghavami, O. Holderer, C. Scherzinger, P. Lindner, W. Richtering, D. Richter and R. G. Winkler, *Macromolecules*, 2016, **49**, 3608–3618.
- 41 A. Ghavami, H. Kobayashi and R. G. Winkler, *J. Chem. Phys.*, 2016, **145**, 244902.



- 42 B. Sierra-Martin, J. R. Retama, M. Laurenti, A. Fernandez-Barbero and E. Lopez Cabarcos, *Adv. Colloid Interface Sci.*, 2014, **205**, 113–123.
- 43 M. U. Witt, N. Möller, S. Backes, S. Hinrichs, B. Fischer and R. V. Klitzing, *J. Phys. Chem. B*, submitted.
- 44 R. H. Pelton and P. Chibante, *Colloids Surf.*, 1986, **20**, 247–256.
- 45 S. Schmidt, M. Zeiser, T. Hellweg, C. Duschl, A. Fery and H. Möhwald, *Adv. Funct. Mater.*, 2010, **20**, 3235–3243.
- 46 H. Hertz, *Reine Angew. Math.*, 1881, **92**, 156–171.
- 47 V. Tsukruk, A. Sidorenko, V. Gorbunov and S. Chizhik, *Langmuir*, 2001, **17**, 6715–6719.
- 48 M. E. Harmon, D. Kuckling, P. Pareek and C. W. Frank, *Langmuir*, 2003, **19**, 10947–10956.
- 49 J. Wiedemair, M. J. Serpe, J. Kim, J.-F. Masson, L. A. Lyon, B. Mizaikoff and C. Kranz, *Langmuir*, 2007, **23**, 130–137.
- 50 M. Ohl, M. Monkenbusch, N. Arena, T. Kozielski, G. Vehres, C. Tiemann, M. Butzek, H. Soltner, U. Giesen, R. Achten, B. Lindenau, A. Budwig, H. Kleines, M. Drochner, P. Kaemmerling, M. Wagner, R. Moller, E. B. Iverson, M. Sharp and D. Richter, *Nucl. Instrum. Methods Phys. Res., Sect. A*, 2012, **696**, 85–99.
- 51 O. Holderer, M. Monkenbusch, R. Schätzler, H. Kleines, W. Westerhausen and D. Richter, *Meas. Sci. Technol.*, 2008, **19**, 034022.
- 52 P. N. Pusey, in *Neutrons, X-rays and Light: Scattering Methods Applied to Soft Condensed Matter*, Introduction to Scattering Experiments, ed. P. Lindner and T. Zemb, Elsevier, 2002, pp. 3–21.
- 53 D. Sivia, *Elementary Scattering Theory*, Oxford University Press, 2011.
- 54 M. Rubinstein and R. H. Colby, *Polymer Physics*, Oxford University Press, 2003.
- 55 M. J. Hore, B. Hammouda, Y. Li and H. Cheng, *Macromolecules*, 2013, **46**, 7894–7901.
- 56 G. Yuan, X. Wang, C. C. Han and C. Wu, *Macromolecules*, 2006, **39**, 3642–3647.
- 57 U. Zettl, S. T. Hoffmann, F. Koberlin, G. Krausch, J. Enderlein, L. Harnau and M. Ballauff, *Macromolecules*, 2009, **42**, 9537–9547.
- 58 M. Shibayama, T. Norisuye and S. Nomura, *Macromolecules*, 1996, **29**, 8746–8750.
- 59 M. Shibayama, *Macromol. Chem. Phys.*, 1998, **199**, 1–30.
- 60 M. Shibayama, *Bull. Chem. Soc. Jpn.*, 2006, **79**, 1799–1819.
- 61 P.-G. de Gennes, *Scaling Concepts in Polymer Physics*, Dynamics of Gels, Cornell University Press, 1979, pp. 215–217.
- 62 D. Richter, M. Monkenbusch, A. Arbe and J. Colmenero, *Neutron Spin Echo in Polymer Systems*, Springer, 2005.
- 63 A. Mourran, Y. Wu, R. A. Gumerov, A. A. Rudov, I. I. Potemkin, A. Rich and M. Möller, *Langmuir*, 2016, **32**, 723–730.
- 64 M. F. Schulte, A. Scotti, A. P. Gelissen, W. Richtering and A. Mourran, *Langmuir*, 2018, **34**, 4150–4158.
- 65 A. Burmistrova, M. Richter, M. Eisele, C. Üzüüm and R. von Klitzing, *Polymers*, 2011, **3**, 1575–1590.
- 66 M. Urich and A. R. Denton, *Soft Matter*, 2016, **12**, 9086.
- 67 A. Meier-Koll, V. Pipich, P. Busch, C. M. Papadakis and P. Müller-Buschbaum, *Langmuir*, 2012, **28**, 8791–8798.
- 68 T. Hellweg, K. Kratz, S. Pouget and W. Eimer, *Colloids Surf., A*, 2002, **202**, 223–232.
- 69 Y. Doi and M. Tokita, *Langmuir*, 2005, **21**, 9420–9425.
- 70 M. Tokita and T. Tanaka, *J. Chem. Phys.*, 1991, **95**, 4613–4619.
- 71 M. Tokita, *Polymers*, 2014, **6**, 651–666.
- 72 F. Tanaka, T. Koga, H. Kojima and F. M. Winnik, *Macromolecules*, 2009, **42**, 1321–1330.
- 73 H. Kojima, F. Tanaka, C. Scherzinger and W. Richtering, *J. Polym. Sci., Part B: Polym. Phys.*, 2013, **51**, 1100–1111.
- 74 F. M. Winnik, *Macromolecules*, 1990, **23**, 233–242.
- 75 Y. Ono and T. Shikata, *J. Am. Chem. Soc.*, 2006, **128**, 10030–10031.
- 76 K. Kubota, S. Fujishige and I. Ando, *Polym. J.*, 1990, **22**, 15–20.
- 77 M. Malmsten, H. Bysell and P. Hansson, *Curr. Opin. Colloid Interface Sci.*, 2010, **15**, 435–444.

